

# Coherent Azimuth Ambiguity Suppression Based on Linear Optimum Filtering of Short Along-Track Baseline SAR Interferograms

Dominik Richter<sup>a</sup>, Marc Rodriguez-Cassola<sup>a</sup>, Mariantonietta Zonno<sup>a</sup>, and Pau Prats-Iraola<sup>a</sup>

<sup>a</sup>German Aerospace Center (DLR), Oberpfaffenhofen, Germany

## Abstract

We propose a coherent ambiguity suppression algorithm for short-baseline interferometric systems with modest ambiguity rejection capabilities, typically suited for companion SAR missions. The algorithm leverages different looks of an interferogram to achieve multilooking and ambiguity suppression. Applying different window functions to SAR images allows to modulate the azimuth ambiguity to signal ratio (AASR). The interferograms with different AASRs are then combined such that the mean square error is minimized, which provides good ambiguity suppression performance and tolerance to common phase and amplitude calibration errors.

## 1 Introduction

Companion Synthetic Aperture Radar (SAR) extensions offer the possibility to enhance existing missions with single-pass interferometric capabilities. Companion satellites are typically receive-only simplified versions of the accompanied system, using smaller platforms and antennas. This results in modest ambiguity rejection capabilities when compared to their full-performance counterparts. An example is ESA's Explorer 10 candidate mission Harmony [1], which uses along-track interferometry (ATI) [2] with a short-baseline in the order of a few meters and requires an interferometric phase estimation accuracy well below 1 deg.

The impact of correlated ambiguities in SAR interferograms was analyzed in [3]. The removal of azimuth ambiguities from interferograms has been proposed by using an iterative equalizer by López-Dekker et. al. [4]. The algorithm in [4] assumes a stable behavior of the interferometric signatures beyond the synthetic aperture time, which might limit its applicability when imaging non-stationary areas.

We propose in this paper a removal scheme at interferogram level, which leverages differences in ambiguity signatures from multiple interferograms to separate main and ambiguous parts.

## 2 Problem Statement

Let us assume our SAR system modulates the return of the imaged scene signal with a similar weighting as the one shown in Fig. 1. The figure shows in blue the weighting of the signal of interest and in red and green the weighting of the ambiguous returns. By applying the windows shown in Fig. 2 to the focused images, those variations will modulate the ratios between ambiguous and main signal power within the image as listed in Tab. 1.

It is possible to spread the azimuth ambiguity to signal

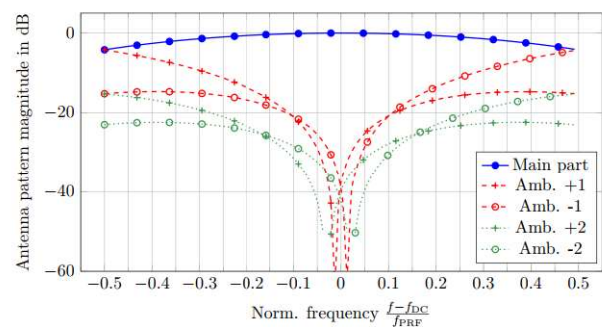


**Figure 1** Exemplary spectral signal and alias magnitude of a SAR system

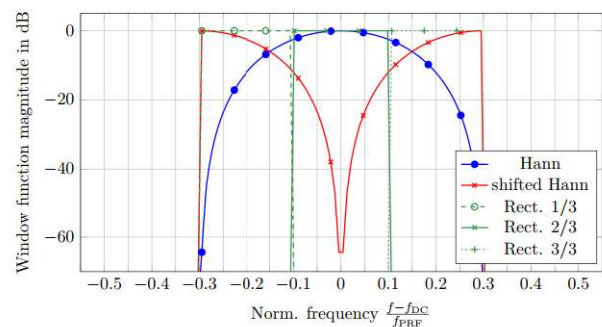


**Figure 2** Exemplary window functions

ratio (AASR) for the first ambiguity within a range of 13.5 dB and the second ambiguity by 12.4 dB. We will use the different signatures of ambiguities in each interferogram to estimate and suppress the ambiguous power.

The algorithm is implemented by means of a linear filter; unlike [4], it does not require interferometric data from the positions of ambiguities and is therefore more robust with respect to the temporal stability of the observed surface.

When assessing the performance with static scenes the suggested approach shows a lower sensitivity to amplitude



Window function	AASR in dB for ambiguity			
	-2	-1	+1	+2
Flat	-24.55	-15.71	-15.68	-24.6
Hann	-30.59	-22.21	-22.19	-30.52
shifted Hann	-21.55	-12.59	-12.57	-21.62
Rect. 1/3	-23.9	-16.27	-12.46	-22.24
Rect. 2/3	-33.97	-25.98	-25.97	-33.69
Rect. 3/3	-22.04	-12.51	-16.3	-23.75

**Table 1** AASR for first two ambiguities using different window functions.

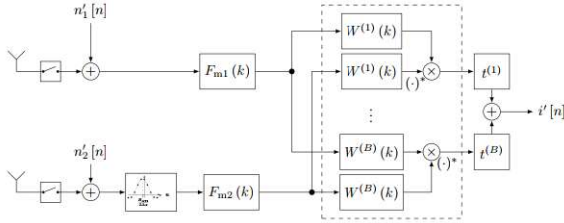


**Figure 3** Block diagram of data processing for ambiguity suppression using several window functions.

and phase errors compared to the IIR equalizer in [4], at the expense of a small degradation in the ambiguity suppression performance. This includes the absolute knowledge of interferometric along-track baseline, hence the phase of the interferometric complex ambiguity to signal ratio [5].

### 3 Interferometric data model

The present subsection describes the signal model for the derivation of the algorithm. Firstly, two SAR channels with a mutual along-track baseline are focused and the second channel co-registered to the first channel as shown in Fig. 3. The azimuth spectra of the two images are separately weighted with  $B$  different window functions  $W^{(b)}(k)$ , where  $k$  is the azimuth wavenumber. This produces an interferometric pair associated to each window function, i.e.,

$$\begin{aligned} \mathbf{u}^{(b)}[n] &= \begin{bmatrix} u_1^{(b)}[n] + n_1^{(b)}[n] \\ u_2^{(b)}[n] + n_2^{(b)}[n] \end{bmatrix} \\ &= \beta_1^{(b)} \sum_{i=-\infty}^{\infty} \left[ \sqrt{\beta_2^{(b)}} \alpha_{1,i}^{(b)} \Gamma_i^{(b)}[n] \right] + \begin{bmatrix} n_1^{(b)}[n] \\ n_2^{(b)}[n] \end{bmatrix}, \end{aligned} \quad (1)$$

where  $n_1$  and  $n_2$  denote additive noise,  $i$  indexes the different signal parts (with  $i = 0$  being the main signal and  $i \neq 0$  being the ambiguities),  $\Gamma_i^{(b)}[n]$  denotes the complex reflectivity of the scene,  $\phi_i$  is the interferometric phase,  $\beta_1^{(b)}$  and  $\beta_2^{(b)}$  are real-valued scaling factors and  $\alpha_{1,i}^{(b)}$  and  $\alpha_{2,i}^{(b)}$  are complex-valued factors such that  $|\alpha_{1,i}^{(b)}|^2$  and  $|\alpha_{2,i}^{(b)}|^2$  are ambiguity to signal ratios of the  $i$ -th ambiguity for window  $b$  in images 1 and 2, respectively; note  $\alpha_{1,i}^{(b)} \cdot \alpha_{2,i}^{(b)*}$ , where  $*$  denotes complex conjugate, represents the com-

plex ambiguity to signal ratio in the interferogram

$$i^{(b)}[n] = \left( u_1^{(b)}[n] + n_1^{(b)}[n] \right) \left( u_2^{(b)}[n] + n_2^{(b)}[n] \right)^* . \quad (2)$$

The scene signal is modeled as a zero-mean complex Gaussian process, i.e.,

$$\Gamma_i^{(b)}[n] \sim \mathcal{CN}(0, \sigma_i^0), \quad (3)$$

with cross-correlation

$$\mathbb{E} \left[ \Gamma_{i_1}^{(b_1)}[n_1] \Gamma_{i_2}^{(b_2)*}[n_2] \right] = \begin{cases} \sigma_{i_1}^0 & \text{for } i_1 = i_2 \vee \\ & b_1 = b_2 \vee, \\ 0 & \text{else}; \end{cases} \quad (4)$$

the first condition applies in general because of different spectral support and ambiguities being uncorrelated; the second condition only holds if the windows do not share any common spectral support; the last condition is true for homogeneous areas. The same will later be applied to the range impulse response function. The two additive noise components are also zero mean proper complex Gaussian distributed with variances  $P_{N_1}^{(b)}$  and  $P_{N_2}^{(b)}$  and identical assumptions on cross-correlation. Some assumptions will not hold for real interferograms, i.e. if the spectral support overlaps, but simplifies the algorithm formulation dramatically.

The algorithm combines pixels from  $B$  different interferograms. In general, the interferograms may have different azimuth resolutions  $\Delta_b$  due to the windowing. For the sake of simplicity, we conduct an equalization of the azimuth resolution by applying a boxcar pre-averaging of  $Q^{(b)}$  pixels per range line. Then,  $N$  pixels in range direction are stacked into an interferogram data vector

$$\mathbf{i}^{(b)}[n] = \frac{1}{Q^{(b)}} \sum_{q=1}^{Q^{(b)}} \begin{bmatrix} i^{(b)}[n + q\Delta_b, 1] \\ \vdots \\ i^{(b)}[n + q\Delta_b, N] \end{bmatrix}. \quad (5)$$

Finally, all  $B$  interferogram data vectors are stacked to form the total interferogram vector

$$\mathbf{i}[n] = \begin{bmatrix} \mathbf{i}^{(1)}[n] \\ \vdots \\ \mathbf{i}^{(B)}[n] \end{bmatrix}. \quad (6)$$

The expected interferometric data

$$\mathbb{E}[\mathbf{i} | \sigma^0, \phi] = \mathbf{A}\mathbf{s}, \quad (7)$$

consists of the ambiguity matrix  $\mathbf{A}$ , which contains the modulated complex signal to ambiguity ratios, and the interferometric signal parameters

$$\mathbf{s} = \begin{bmatrix} \sigma_{-\infty}^0 e^{j\phi_{-\infty}} \\ \vdots \\ \sigma_0^0 e^{j\phi_0} \\ \vdots \\ \sigma_{\infty}^0 e^{j\phi_{\infty}} \end{bmatrix}, \quad (8)$$

where only  $\sigma_0^0 e^{j\phi_0}$  is of interest. The other parameters contain information about the interferometric parameters of all ambiguities.



## 4 Linear Minimum Mean Square Error Estimator

### 4.1 Deriving a linear estimator

The interferograms are combined in terms of a Linear Minimum Mean Square Error (LMMSE) estimator

$$\hat{s} = T\mathbf{i} + \mathbf{m}, \quad (9)$$

which minimizes the Mean Square Error (MSE) [6]

$$T, \mathbf{m} = \arg \min_{T, \mathbf{m}} \mathbb{E} \left[ |\mathbf{s} - T\mathbf{i} - \mathbf{m}|^2 \right] \quad (10)$$

$$= \arg \min_{T, \mathbf{m}} \mathbb{E} \left[ |\mathbf{s} - T(\mathbf{A}\mathbf{s} + \mathbf{v}) - \mathbf{m}|^2 \right], \quad (11)$$

where all variations of the interferogram data about its expected value due to thermal noise and speckle [7] are combined into a noise vector

$$\mathbf{v} = \mathbf{i} - \mathbf{A}\mathbf{s}. \quad (12)$$

The estimator is found to be

$$T = \mathbf{C}_{ss} \mathbf{A}^H (\mathbf{A} \mathbf{C}_{ss} \mathbf{A}^H + \mathbf{C}_{vv})^{-1} \quad (13)$$

$$\mathbf{m} = \mathbb{E}[\mathbf{s}] - T \mathbf{A} \mathbb{E}[\mathbf{s}], \quad (14)$$

where the  $\mathbf{C}_{ss}$  and  $\mathbf{C}_{vv}$  are the covariance matrices for  $\mathbf{s}$  and  $\mathbf{v}$ , respectively. When computing  $\mathbf{C}_{vv}$ , neglecting the cross-correlations of speckle and thermal noise between interferograms is true for interferograms which share no common azimuth bandwidth only, but definitely wrong for interferograms with common bandwidth. For large values of  $Q^{(b)}$ , the covariance matrix for the interferometric signatures will dominate the total noise covariance matrix, which reduces the impact of the cross-correlations of the interferograms in the estimation.

### 4.2 Deriving the complex azimuth ambiguity to signal ratios

Rather than deriving the usual power ratios of  $|\alpha_{1,i}^{(b)}|^2$  and  $|\alpha_{2,i}^{(b)}|^2$ , well known in the literature, [8], [9], we present the computation of the ratios of the complex-valued signals. For a wide-sense stationary scene or approximately also for slowly changing scene, one can derive the value of  $\alpha_{1,i}^{(b)} \alpha_{2,i}^{(b)*}$  as follows

$$\alpha_{1,i}^{(b)} \alpha_{2,i}^{(b)*} = \frac{\int_{k_{DC}-k_{BW}}^{k_{DC}+k_{BW}} H_1(k + ik_{PRF}) F_{m1}(k) W^{(b)}(k) \cdot H_2^*(k + ik_{PRF}) F_{m2}^*(k) W^{(b)*}(k) dk}{\int_{k_{DC}-k_{BW}}^{k_{DC}+k_{BW}} H_1(k) F_{m1}(k) W^{(b)}(k) H_2^*(k) F_{m2}^*(k) W^{(b)*}(k) dk}, \quad (15)$$

where  $k_{PRF}$  is the pulse repetition frequency,  $k_{DC}$  the Doppler centroid and  $k_{BW}$  the processed bandwidth, for consistency all scaled into wavenumbers;  $H_1(k)$  and  $H_2(k)$  denote the azimuth spectra of the SAR data, and  $F_{m1}(k)$  and  $F_{m2}(k)$  are phase-only focusing kernels.

Wind speed in m/s	Exp. RCS E $[\sigma^0]$ in dB	Shape parameter $k$	Scale parameter $\theta$
3.78	-5.9	3.46	0.0743
10.53	-11.8	2.58	0.0256
15.23	-19.7	2.61	0.0041

**Table 2** Shape and scale parameter of Gamma distributed ground reflectivity for different wind conditions.

## 5 Experimental results

### 5.1 Parameter distributions for Monte Carlo runs

The ground reflectivity parameters are assumed to be independently Gamma distributed [10]

$$\sigma^0 = \sigma_{-\infty}^0, \dots, \sigma_0^0, \dots, \sigma_{\infty}^0 \sim \Gamma(k, \theta) \quad (16)$$

according to the scene reflectivity condition, which have been derived from Sentinel-1 data in wave mode for different wind conditions, as shown in Tab. 2.

We further assume the interferometric phases are independent and uniformly distributed within a maximum variation of the Doppler velocity of  $\pm 90$  cm/s.

$$\phi = \phi_{-\infty}, \dots, \phi_0, \dots, \phi_{\infty} \sim \mathcal{U}(\pm s_I 90 \text{ cm/s}), \quad (17)$$

where  $s_I$  denotes the interferometric sensitivity [2] of the ATI-SAR system.

### 5.2 Simulation model

In order to prove the ability of the suggested algorithm to achieve a reasonable ambiguity suppression, a one-dimensional model is used. It considers the azimuth impulse response function and the effect of co-registration on coherent ambiguities [5]. Furthermore, cross-correlations, which will occur in real interferograms but have been neglected in the model formulation in (4), are present in the simulated data. Multiple range lines are simulated by using several independent realizations of the one-dimensional azimuth model.

The offset of the phase error curve in a double logarithmic plot is determined by the coherence, which may be found according to [3]. The curve shows a linear slope over the number of samples as expected from [11]

$$\sigma_{\phi} = \sqrt{\frac{1 - |\gamma|^2}{2N |\gamma|^2}}, \quad (18)$$

where  $N$  is the number of averaged samples. Low backscatter typically requires high averaging to mitigate thermal noise as shown in Fig. 4 (a) to (c). With a sufficiently large number of averaging pixels, the uncorrected interferometric phase shows biases due to ambiguities, which do not decrease with more averaging. The implemented LMMSE algorithm achieves similar suppression performance compared to the IIR equalizer in [4]. For an increasing number of averaging pixels, the phase error percentiles of the data corrected with our LMMSE algorithm appear slightly higher, a consequence of the use of the windows to spread the ambiguity to signal ratios.



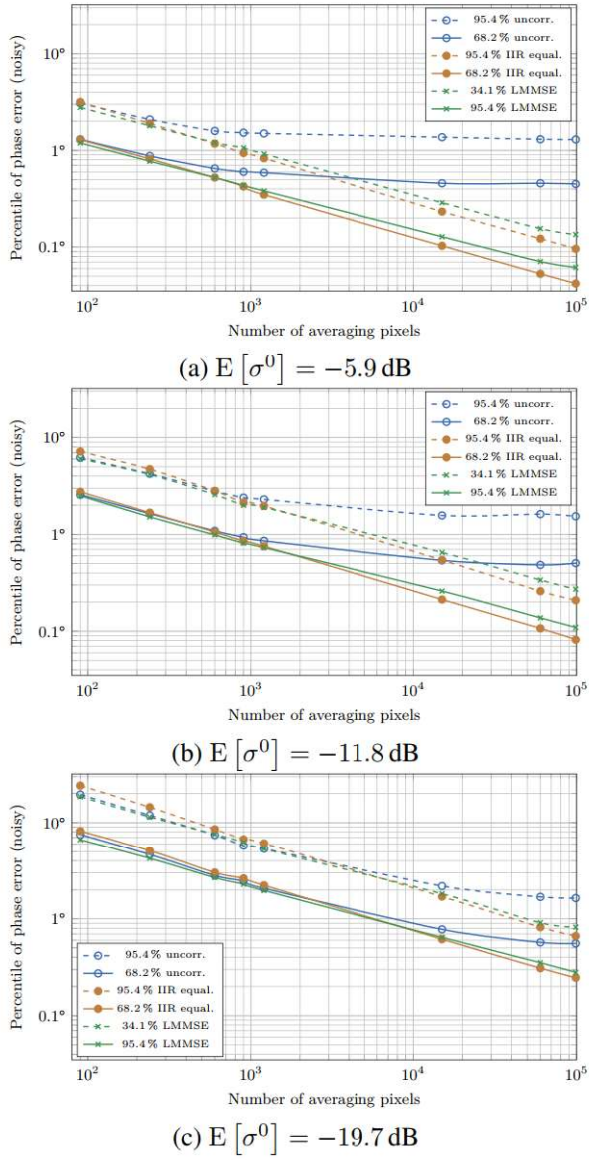


**Figure 4** Percentiles of phase error caused by 3 left and 3 right ambiguities, for scenes with different expected RCS and  $\sigma_{NE}^0 = -20 \text{ dB}$  before and after applying suppression algorithms, DPCA condition is fulfilled and 28 window functions are applied.

### 5.3 Sensitivity analysis

To study the sensitivity of azimuth ambiguity suppression algorithms to the phase knowledge of the complex ambiguity to signal ratio, we introduce an along-track baseline error in our model between  $\pm 8 \%$ , which induces a variation of phase of the complex ambiguity to signal ratio of  $\pm 28.62 \text{ deg}$ . Fig. 5 shows the variation of the performance of the algorithms as a function of the relative baseline error. It can be seen that the performance of the IIR equalizer degrades beyond  $1 \%$ , whereas that of the LMMSE approach stays constant. The reason for this independence with the baseline error is due to the fact that the error is common to all interferograms formed by different window functions, i.e., the phase error due to the baseline knowledge is absorbed in the estimation of ambiguous signals. The effect of antenna phase pattern variations on algorithm sensitivity

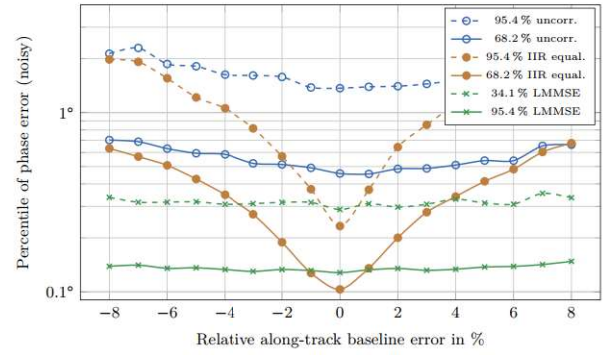


**Figure 5** Percentiles of phase error caused by 3 left and 3 right ambiguities over along-track baseline error for an expected RCS of  $-5.9 \text{ dB}$ ,  $\sigma_{NE}^0 = -20 \text{ dB}$  and averaging 15000 pixels, before and after applying suppression algorithms, DPCA condition is fulfilled in  $0 \%$  error case and 28 window functions are applied.

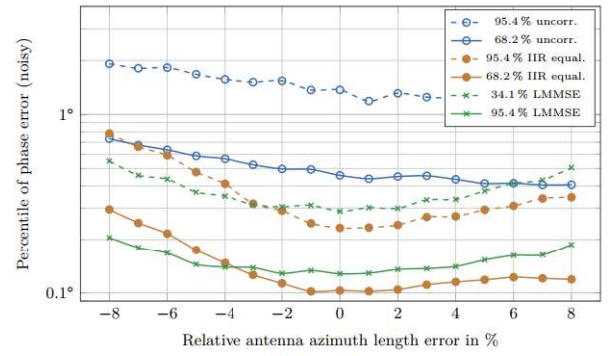


**Figure 6** Percentiles of phase error caused by 3 left and 3 right ambiguities over antenna length error for an expected RCS of  $-5.9 \text{ dB}$ ,  $\sigma_{NE}^0 = -20 \text{ dB}$  and averaging 15000 pixels, before and after applying suppression algorithms, DPCA condition is fulfilled in  $0 \%$  error case and 28 window functions are applied.

are subject to further investigations.

By varying the antenna length of our model we investigate the algorithm sensitivity to the variation of the magnitude of the  $\Lambda \text{ASR}$ . When sweeping the antenna length within  $\pm 8 \%$ , one observes a variation of the first ambiguity to signal ratio (with  $i = \pm 1$ ) for a flat window function from  $1.65 \text{ dB}$  to  $-0.81 \text{ dB}$ . The effect of the error caused by a broadening/shrinking of the pattern due to the imperfect knowledge of antenna length on the performance of the ambiguity suppression is shown in Fig. 6. In case of the LMMSE algorithm, one finds a comparable sensitivity of ambiguity suppression within  $\pm 8 \%$ , where the variation of the first ambiguity to signal ratio is confined within  $-5.74$  to  $8.87 \text{ dB}$ . The LMMSE algorithm depends on a larger set of different ambiguity to signal ratios, which all have different sensitivity to antenna length variation. The dependence is more complex and determined by the sensitivity of each ratio with respect to the antenna length knowledge. Nevertheless, we find similar behavior for both algorithms.

We presented a multi-interferogram LMMSE algorithm that removes ambiguities by weighting different looks of an interferometric scene. By forming several interferograms from images with different window functions during image processing, the AASR apparent for the interferogram is varied. These variations, together with the knowledge on the antenna patterns, are used to estimate the contributions of ambiguities to the interferograms. The scheme is especially suited to short-baseline interferometric systems with modest ambiguity rejection capabilities. We have shown in this paper that the suggested algorithm does not impose longer temporal stability on the signatures of the ambiguities and is capable of coping with common phase error sources.

## 7 Literature

- [1] P. López-Dekker, H. Rott, P. Prats-Iraola, B. Chapron, K. Scipal, E. De Witte: Harmony: An Earth Explorer 10 mission candidate to observe land, ice, and ocean surface dynamics, Yokohama: IGARSS 2019, 2019
- [2] R. M. Goldstein, H. A. Zebker: Interferometric Radar Measurement of Ocean Surface Currents, Vol. 328, Nature, 1987, pp. 707-709
- [3] M. Villano, G. Krieger: Impact of Azimuth Ambiguities on Interferometric Performance, Vol. 9 No. 5, IEEE Geoscience and Remote Sensing Letters, 2012, pp. 896-900
- [4] P. López-Dekker, Y. Li, L. Iannini, P. Prats-Iraola, M. Rodriguez-Cassola: On Azimuth Ambiguities Suppression For Short-Baseline Along-Track Interferometry: The STEREOID Case, Yokohama: IGARSS 2019, 2019
- [5] P. López-Dekker, B. Chapron, H. Johnsen: Observations of Sea Surface Winds and Sea Surface Deformation with the Harmony mission, Leipzig: EUSAR 2021, 2021
- [6] N. Wiener: Extrapolation, interpolation and smoothing of stationary time series, Technology Press of the Mass. Inst. of Technology, Cambridge, 1949
- [7] D. Just, R. Bamler: Phase Statistics of Interferograms with Applications to Synthetic Aperture Radar, Vol. 33, Applied Optics, 1994, pp. 4361-4368
- [8] K. Tomiyasu: Tutorial Review of Synthetic-Aperture Radar with Applications to Imaging of the Ocean Surface, Vol. 66, Proceedings of the IEEE, 1978, pp. 563-583
- [9] F. K. Li, W. T. K. Johnson: Ambiguities in Spaceborne Synthetic Aperture Radar Systems, Vol. AES-19 No. 3, IEEE Transactions On Aerospace and Electronic Systems, 1983, pp. 389-396
- [10] A. Papoulis: Probability, Random Variables, and Stochastic Processes, 4th ed., Boston, McGraw-Hill, 2002
- [11] P. Rosen *et al.*, Synthetic Aperture Radar Interferometry, Proceedings of the IEEE, vol. 88, no. 3, March,